Supplementary Material: A singlet-triplet hole-spin qubit in MOS silicon.

S. D. Liles[1,†], D. J. Halverson[1], Z. Wang[1], A. Shamim[1], R. S. Eggli[2], I. K. Jin[1,3], J. Hillier[1], K. Kumar[1], I. Vorreiter[1], M. J. Rendell[1], J. H. Huang[4,5], C. C. Escott[4,5], F. E. Hudson[4,5], W. H. Lim[4,5], D. Culcer[1], A. S. Dzurak[4,5], A. R. Hamilton[1]

[1] *School of Physics, University of New South Wales, Sydney NSW 2052, Australia.*
[2] *Department of Physics, University of Basel, Klingelbergstrasse 82, CH-4056 Basel, Switzerland.*
[3] *Center for Emergent Matter Science, RIKEN, 2-1, Hirosawa, Wako-shi, 351-0198, Saitama, Japan.*
[4] *School of Electrical Engineering and Telecommunications, University of New South Wales, Sydney NSW 2052, Australia.*
[5] *Diraq, Sydney NSW, Australia.*

S1 5x5 Singlet-Triplet Hamiltonian

Here we present full details of the 5x5 Hamiltonian H_{ST}, which is used to model the singlet triplet system. We include the Zeeman Hamiltonian in the form

$$H_z = \frac{\mu_B}{2}((\overleftrightarrow{g}_L \cdot \vec{B}) \cdot \vec{\sigma}_L) \otimes \mathbb{1}_R + \mathbb{1}_L \otimes ((\overleftrightarrow{g}_R \cdot \vec{B}) \cdot \vec{\sigma}_R)) \tag{S1}$$

where $\overleftrightarrow{g}_{L,R}$ are the 3x3 g-tensors for the left and right dot, μ_B is the Bohr magneton, $\vec{B}$ is the magnetic field with respect to the lab (x,y,z) frame, and $\vec{\sigma}_{L,R}$ are the pauli vectors for the left and right dot. We make no prior assumptions that $\overleftrightarrow{g}_L$ or $\overleftrightarrow{g}_R$ are diagonalizable in the same eigenbasis, allowing each g-tensor to exhibit independent anisotropy. This is equivalent to allowing the principle axes of each g-tensor to be independent. As a result, and for convenient comparison with the experiment, we define $\vec{B}$ in the lab frame of reference.

Using these conventions the g-tensor in the lab frame-of-reference is defined as,

$$\overleftrightarrow{g}_i = \begin{pmatrix} g^i_{xx} & g^i_{xy} & g^i_{xz} \\ g^i_{xy} & g^i_{yy} & g^i_{yz} \\ g^i_{xz} & g^i_{yz} & g^i_{zz} \end{pmatrix} \tag{S2}$$

where i indicates L or R for the left and right dot. The magnetic field is defined as $\vec{B} = (B_x, B_y, B_z)$, where each component is the magnetic field in the lab x,y, and z-axes respectively (see Figure 1a of main text for orientation). Consequently, the term in the Zeeman Hamiltonian ($\overleftrightarrow{g}_i \cdot \vec{B}$) is evaluated as,

$$\overleftrightarrow{g}_i \cdot \vec{B} = \begin{pmatrix} g^i_{xx}B_x + g^i_{xy}B_y + g^i_{xz}B_z \\ g^i_{xy}B_x + g^i_{yy}B_y + g^i_{yz}B_z \\ g^i_{xz}B_x + g^i_{yz}B_y + g^i_{zz}B_z \end{pmatrix}. \tag{S3}$$

In the main text, we define the difference in the Zeeman energy between the left and right dot as

$$\Delta E_z = |\Delta g^*| \mu_B |\vec{B}| \tag{S4}$$

where $\Delta g^* = g^*_L - g^*_R$, and $g^*_{L,R}$ are the effective g-factors of the left and right dot respectively. The effective g-factor is the g-factor the is observed for a specific magnetic field orientation and can be evaluated from the respective g-tensor as,

$$g^*_i = \frac{|\overleftrightarrow{g}_i \cdot \vec{B}|}{|\vec{B}|}. \tag{S5}$$

We include a spin-orbit Hamiltonian of the form,

$$H_{so} = (\vec{t}_{so} \cdot \vec{\sigma}_L) \otimes \mathbb{1}_R + \mathbb{1}_L \otimes (\vec{t}_{so} \cdot \vec{\sigma}_R) \tag{S6}$$

where the spin-orbit vector is defined by components in the lab frame such that $\vec{t}_{so} = (t_x, t_y, t_z)$.

† Corresponding author - s.liles@unsw.edu.au

Finally, we include the orbital Hamiltonian in the standard form,

$$H_{orb} = \epsilon \left|S_{2,8}\right\rangle \left\langle S_{2,8}\right| + \sqrt{2}t_c(\left|S\right\rangle \left\langle S_{2,8}\right| + \left|S_{2,8}\right\rangle \left\langle S\right|) \tag{S7}$$

where ϵ is the detuning energy and t_c is the tunnel coupling between the left and right dot.

The full 5x5 model for the two-hole singet-triplet system is then given by

$$H_{ST} = H_z + H_{so} + H_{orb}. \tag{S8}$$

S2 Extended characterisation measurements

S2.A Temperature effects

In Figure S1a-c) we show singlet-triplet oscillations measured at 214 mK, 441 mK and 834 mK respectively. The measurements shown are for $B_x = 15$ mT and data up to 300 ns is presented, however all data was measured up to 500 ns for accurate extraction of T_2^*. In each case the data was fit to the equation shown in the inset of c). This equation is equivalent to Eqn. 4 of the main text, with the condition that ΔI has been converted to P_S based on the normalisation described above. Figures S1d-f) show the extracted fitting parameters for data measured at a range of different mixing chamber temperatures. We note that the maximum amplitude 'A' decreases steadily with T_{MC}, starting from base temperature, and dropping to a minimum around 800 mK. This is distinctly different to the T_2^* data, which remains constant up to around 400 mK. We suspect the decrease in 'A' is related to a suppression of the visibility of the latched readout. We suggest this may occur as thermal effects equalise the left and right tunneling rates.

Figure S1e) shows the fit parameter α, which is related to the spectral colour of the noise. If the noise power follows a power law, then the noise power is given by $S(f) \propto f^{-\beta}$ and the decay envelope for coherent oscillations is given by $\exp(-\tau/T_2^*)^{\beta+1}$. We define $\alpha = \beta + 1$, such that $\alpha = 2$ ($\beta = 1$) corresponds to the usual 1/f noise spectrum. Figure S1e) shows value of α obtained for a best fit of the experimental data to the equation displayed in the inset. The data in Figure S1e) shows α decreasing towards 1 as the temperature increases. Previous experiments in other systems have noted that α shows temperature dependence, with the noise tending to become 'whiter' (ie $\alpha \to 1$) as the temperature increases[1]. The exact mechanism for this change in spectral noise is unclear. Figure S1e) shows that α tends towards 1 as the temperature increases.

For all fitting in the main text we made the assumption that 1/f noise is the dominant noise source, and fixed $\alpha = 2$ to simplify the fitting. To ensure this assumption of $\alpha = 2$ doesn't influence the fitting parameters, we performed fitting with a free α and a fixed $\alpha = 2$. Figures S1d) and f) show the best fit value of A and 'T_2^*' extracted using fixed α and free α. In both cases the free choice of α is within the error bars of the fitting, indicating that the values of these fit parameters are reasonably robust against changes in α.

Finally, Figure S1g) shows the extracted singlet-triplet oscillation frequency as a function of mixing chamber temperature. We observe a reproducible shift in the oscillation frequency of 6 MHz as the temperature is increased. We are confident this is not a slow drift in the oscillation frequency since the data were collected in semi-random order.

S2.B Full 2π characterisation

Figure S2a) shows the measurement of Figure 2c) extended to a full 2π rotation in-plane. Clear anisotropic oscillations can be observed in the sensor signal. For τ_S less than 4 ns no clear signal is observed. This is due to the effective rise time of the separation pulse. Figure S2b) shows the FFT of the measurement, demonstrating the anisotropy of the eigenstates. These data were obtained using the same pulse sequence used in Figure 2c), which involves an initialisation in S(2,8), a separation pulse to $\epsilon = 1.9$ meV, a dwell at the separation point for time τ_S, and a final pulse to the readout position in order to map the resulting singlet or triplet spin state to the corresponding (2,8) or (2,9) latched charge states.

S3 Model Hamiltonian and simulation of spin dynamics

The Hamiltonian for the hole double quantum dot is defined in Eqn. S8. This Hamiltonian is defined in the basis of $(\left|T_+\right\rangle, \left|T_0\right\rangle, \left|T_-\right\rangle, \left|S\right\rangle, \left|S_{(2,8)}\right\rangle)$. The model Hamiltonian in used in two ways to interpret the experimental

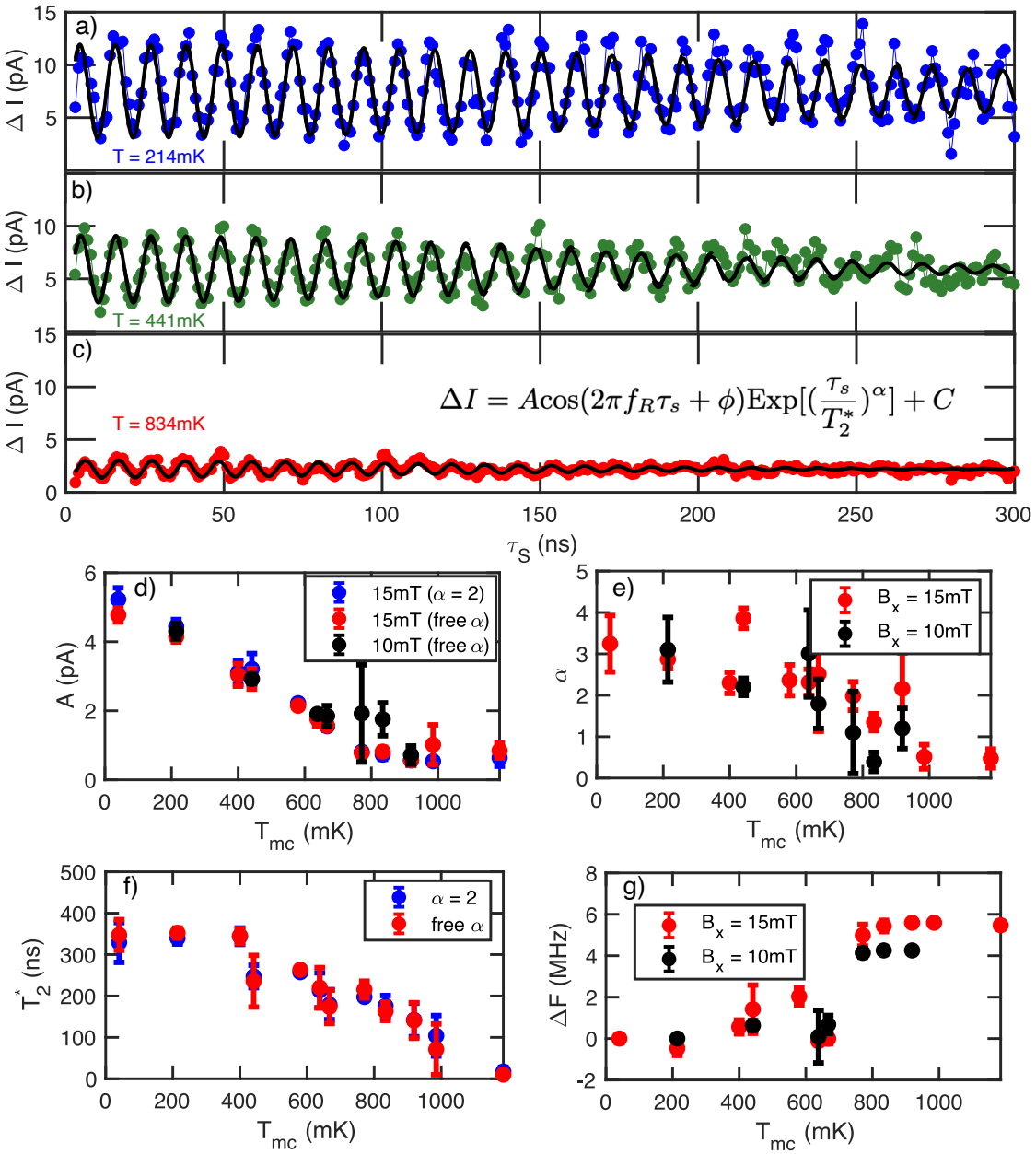

Figure S1: **Additional analysis of singlet-triplet oscillation fitting parameters**. a-c) Charge sensor signal as a function of separation dwell time (τ_S) when using the pulse sequence described in Figure 3 of the main text. The measurement is presented at three different mixing chamber temperatures, 214 mK (blue), 441 mK(green), and 834 mK (red). The oscillations in ΔI are Δg-driven singlet-triplet oscillations. The solid black line is a best fit of the data to the equation shown in the inset of c). For each data sets, we present two fits. The solid line shows the best fit where $\alpha = 2$. Additionally, a second fit is shown in black dashed line, which is the fit where α is left as a free parameter. However, both fits ($\alpha = 2$ and α free) are so similar that it is difficult to see the dashed black line. For each measurement the full data set extends to 500 ns. d) We plot the value of A extracted for a best fit to oscillations at a range of different mixing chamber temperatures. We have extracted A for fits where $\alpha = 2$ and where α was allowed to be free. Overlap between the two data sets indicates that the value of α does not influence the fit parameter A. e) Best fit value of α extracted from oscillations observed at a range of different mixing chamber temperatures. A trend of $\alpha \to 1$ can be observed as temperature increases. f) Comparison of the best fit coherence time for free and fixed α. This demonstrates that the choice of α does not influence the best fit T_2^*. g) The shift in oscillation frequency with respect to the base temperature measurement ($f_R(T_{mc}$= 30 mK) = 30 MHz).

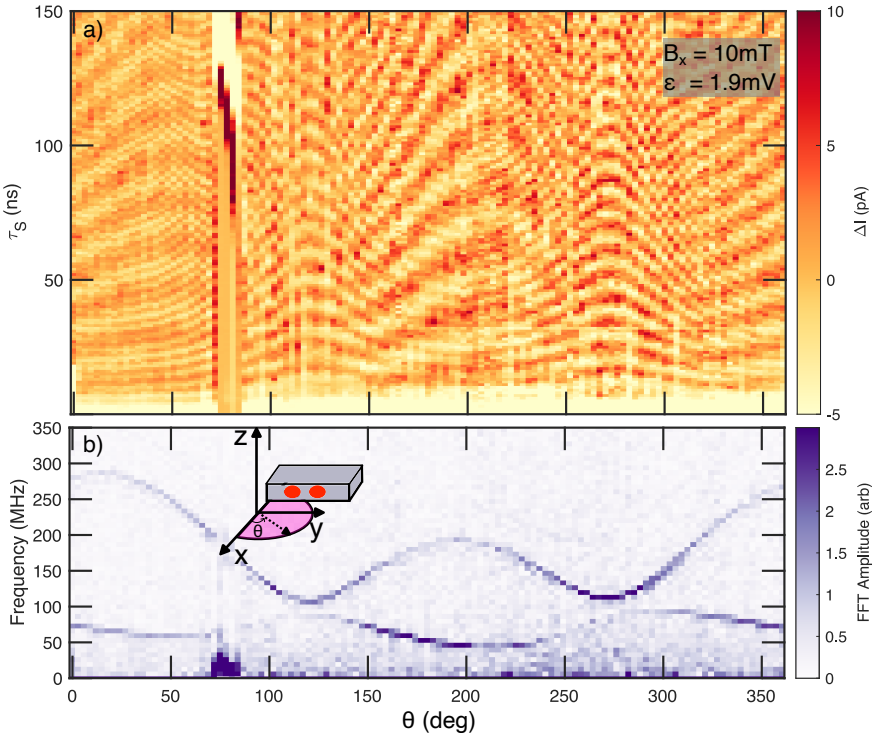

Figure S2: **2π characterisation of in-plane eigenstate anisotropy**. a) The measurement procedure is the same as that using in Figure 2b) of the main text (I-S-R), however here the experiment is performed over a full 2π rotation in-plane. The y-axis shows the separation time and the x-axis indicates the orientation of the magnetic field. Colour scale shows the sensor lock-in signal (ΔI) where several sets of oscillations can be extracted. A shift is the sensor occurred between $\theta = 65^\circ$ and 80°, resulting in the spurious signal over this range. b) Shows a FFT of the ΔI at each magnetic field orientation.

data. Firstly, by solving the eigenstates it is possible to determine the expected energy splittings between each level. The predicted level splitting can be compared with the observed oscillation frequency (ie in Figure 2a-d) in order to determine a best fit for the input parameters. In addition, we have implemented a simulation protocol which models the dynamics of a hole-spin following the experimental pulse sequence and including the full Hamilton. This simulation protocol is used to evaluate the probability of loading the leakage states discussed in Figure 2f).

The key parameters for the Hamiltonian are $\overleftrightarrow{g}_L$, $\overleftrightarrow{g}_R$, $\vec{t}_{so} = (t_x, t_y, t_z)$, and t_c. We consider arbitrary symmetric g-tensors, hence overall this produces 16 free parameters in the model for H_{ST} (Eqn. S8). As shown in Figure 2a-d) of the main text it is possible to observe three independent oscillation frequencies. The best fit procedure uses the anisotropy of the three level splittings to obtain a best fit to the 16 free parameters. We find that H_{ST} (Eqn. S8) provides an excellent fit to the experimental data. However, as a result of the large number of free parameters, when fitting the observed frequencies in Figure 2 to H_{ST}, we are unable to obtain a unique fit. Indeed, we determine that there is a wide range of possible g-tensors and spin-orbit combinations, which provide a good fit to the data.

In order to obtain an optimal fit to the data we consider both the 3 observed FFT frequencies (to obtain best fit parameters), and the FFT amplitude (to assess if the fit parameters support the observed spin-dynamics). As discussed in the main text the FFT amplitude of higher frequency oscillations (ie $|T-\rangle$-$|S\rangle$ oscillations) is dependent on the probability of accessing the $|T-\rangle$ state during the ramp in. Therefore, we also compare the experimental FFT amplitudes with the simulated probability of loading the $|T-\rangle$ state.

We model the spin dynamics of the experiment using the python QuTIP package[2]. Typical simulation protocol starts by defining the initial state, $\Psi(t=0)$ as the lowest energy state at large negative detuning ($\Psi(t=O) = |S_{2,8}\rangle$). We simulate a linear ramp from the initial detuning to a positive detuning value, a hold at the positive detuning and a final ramp back to initial detuing. At each increment during this procedure we project the time evolved $\Psi(t)$ back onto the basis states ($|T_+\rangle, |T_0\rangle, |T_-\rangle, |S\rangle, |S_{(2,8)}\rangle$) to analyse the evolution of the state.

Figure S3a) reproduces the eigenstates of the optimal fit parameters determined in Figure 2 of the main text. To simulate the spin dynamics we model a 4 ns linear ramp in detuning from ϵ =-2 meV to ϵ =1.9 meV (performed for B_x=10 mT). Figure S3b) shows the projection of $\Psi(t)$ onto basis states throughout the ramp. Initially $\Psi(t)$ is primarily $|S_{(2,8)}\rangle$ as defined by initialisation. However, as the ramp moves to positive detuning, $\Psi(t)$ evolves into a mix of $|S\rangle$ and $|T_0\rangle$, which are the operating states of the singlet-triplet qubit. However, there is some residual probability that the $\Psi(t)$ state evolves into the leakage states. As discussed in the main text, the likely hood of accessing these leakage states is related to the probability of making an adiabatic transition of either the $\Delta_{ST\_}$ avoided crossing (for $|T_+\rangle$ and $|T_-\rangle$) or the t_c induced avoided cross (for $|S_{2,8}\rangle$).

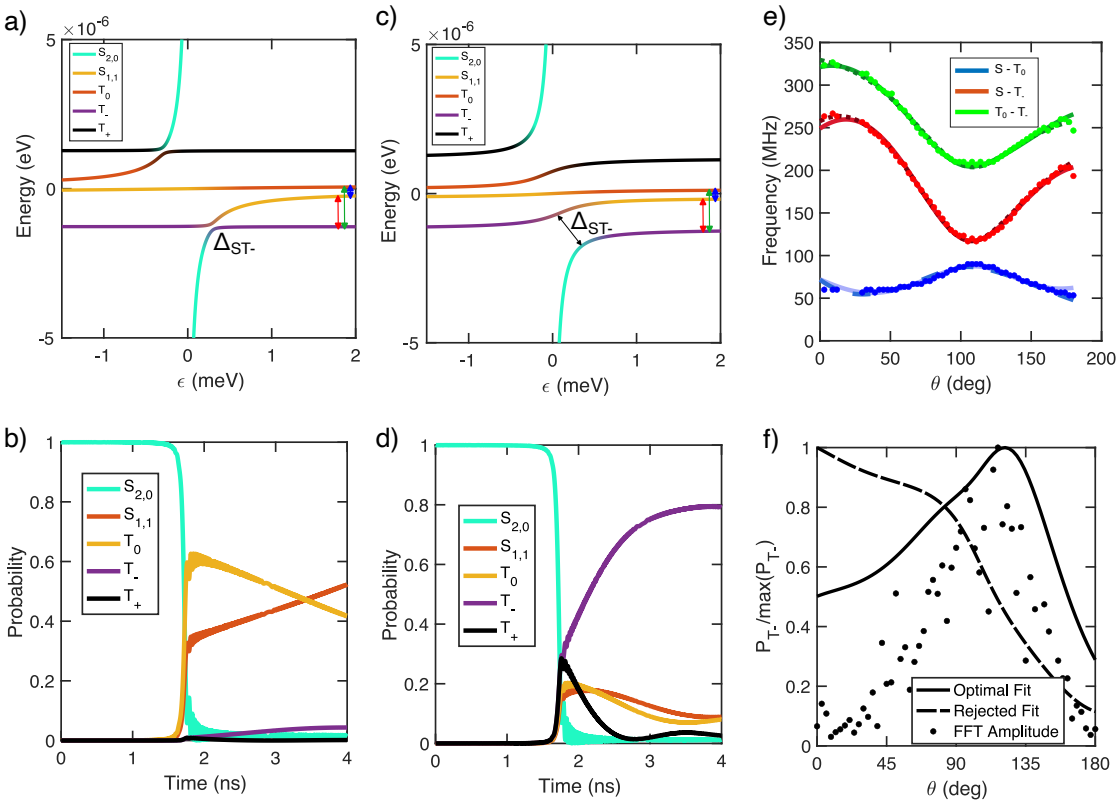

Figure S3: **Modelling the hole-spin dynamics**. a) The eigenenergies are plotted as a function of detuning (ϵ) for the 'optimum' fit parameters (see Table I). b) Probability of occupation of each basis state during a pulse from ϵ=-1.5 meV to ϵ=+1.9 meV. The simulation begins with the system initialised in $|S_{2,0}\rangle$, which transitions into $|S\rangle$ and $|T_0\rangle$ upon crossing $\epsilon = 0$ at 1.8ns. Due to the $\Delta_{ST\_}$ avoided crossing there is a small residual probability of populating the $|T_-\rangle$ leakage state. c) The eigenenergies are plotted as a function of detuning (ϵ) for the 'rejected' fit parameters (see Table I). Here the $\Delta_{ST\_}$ is significantly enhanced due to the large Δg present for the rejected fit parameters. Despite the difference in the $\Delta_{ST\_}$ and the overall parameters, the relative level splittings at $\epsilon = 1.9meV$ are identical between the optimal and rejected fit. This demonstrates the challenge in determining a unique fit using the level splittings alone. d) Probability of occupation of each basis state during a pulse from ϵ = -1.5 meV to ϵ = +1.9 meV. The simulation begins with the system initialised in $|S_{2,0}\rangle$, however for the rejected fit parameters the $|S_{2,0}\rangle$ primarily transitions into the $|T_-\rangle$ when crossing $\epsilon = 0$. e) Circles show the level splitting (in frequency) extracted from the experimental data in FFT data in Figure 2d) of the main text. Solid and dashed lines show the level splitting trend for the 'optimal' (solid) and 'rejected' (dashed) fit parameters. Both fitting parameter sets reproduce the experimental level splitting well. f) Calculated probability of $|S_{2,0}\rangle$ transitioning to $|T_-\rangle$ during the 4 ns separation pulse. The black circles show the amplitude of the experimental $|S\rangle \leftrightarrow |T_-\rangle$ oscillations. For the rejected fit parameters the trend in $P_{T\_}$ is distinctly different to the experimental data, while for the optimal fit the trend in $P_{T\_}$ co responds well with the experimental trend.

S4 Identifying optimal fits

The following section provides a discussion on the full fitting procedure used to identify optimal fitting parameters from the experimental data presented in Figure 2 of the main text. The large number of free parameters in H_{ST} allows many parameter configurations that reproduce the observed anisotropy of the eigenenergies with respect to magnetic field. We constrain the number of fits and identify an 'optimal' fit by additionally considering the anisotropy of the $|S\rangle \leftrightarrow |T_-\rangle$ FFT amplitudes. This is justified since the amplitude of $|S\rangle \leftrightarrow |T_-\rangle$ oscillations is

proportional to the probability of occupying $|T_-\rangle$ (P_{T_-}), which we can calculate P_{T_-} using H_{ST}. In Table I we present the parameters for the 'optimal' fit and an example 'rejected' fit.

Figure S3a) reproduces the eigenenergies of the 'optimal' fit parameters shown in Figure 2 of the main text. Figure S3b) shows the projection of $\Psi(t)$ onto basis states throughout the 4 ns ramp from the initialisation point in (2,8) to the separation point in (1,9). The simulated ramp is linear with initialisation at $\epsilon = -1.5$ meV and separation at $\epsilon = +2$ meV. As the ramp moves to positive detuning, $\Psi(t)$ primarily evolves into a mix of $|S\rangle$ and $|T_0\rangle$, which are the expected operating states of the singlet-triplet qubit. However, there is some small residual probability that the $\Psi(t)$ state evolves into the leakage states.

Figure S3c) shows the eigenenergies of the 'rejected fit' while Figure S3d) shows the result of the ramp-in when using these eigenenergies. We note that for the 'rejected' fit the Δ_{ST_-} avoided crossing is significantly enhanced. This enhancement of Δ_{ST_-} results from the large Δg obtained in the fit parameters. As a result, the ramp-in shown in Figure S3d) results primarily in the loading of the $|T_-\rangle$ state, which is a leakage state for the singlet-triplet qubit. Comparing Figure S3b) and d) demonstrates that although the 'optimal' and 'rejected' fit have equal energy splitting at the separation point, the different fit parameters result in very different dynamics during the ramp-in.

Figure S3e) shows the predicted anisotropy of the level splittings for the 'optimal' (solid) and 'rejected' (dashed) fits for a magnetic field rotation through the x-y plane. The three level splittings shown are the $|S\rangle$-$|T_0\rangle$ (blue), $|S\rangle$-$|T_-\rangle$ (red), and $|T_-\rangle$-$|T_0\rangle$ (green). These are calculated at $\epsilon = 1.9$ meV. Circles of the respective colours show the frequency extracted from the FFT measurements in Figure 2 of the main text. Although the 'optimal' and 'rejected' firs produce significant difference in the ϵ dependence, both reproduce the observed response of the eigenergy splitting to magnetic field orientation. This is because the observed energy splitting is sensitive only to the eigenenergies at the separation point ($\epsilon = 1.9$ meV), and is not influence by the dynamics during the ramp-in.

Figure S3f) shows the simulated $|T_-\rangle$ probability after the 4 ns ramp-in a range of magnetic field orientations around x-y plane. We plot the normalised $|T_-\rangle$ probability, which we define as $P_{T_-}(\theta)/\max(P_{T_-}(\theta))$. The normalised $|T_-\rangle$ probability shows a distinct difference in the anisotropy between the 'optimal' and 'rejected' fits. For comparison, we assume that the amplitude of the experimentally observed $|T_-\rangle$-$|S\rangle$ oscillations is proportional to the probability of loading into the $|T_-\rangle$. Hence, in Figure S3f) we plot the normalised $|T_-\rangle$-$|S\rangle$ oscillation amplitude (extracted from the amplitude of the FFT peaks in Figure 2c). For the 'optimal' fit the trend in P_{T_-} matches the experimental amplitude well, with both exhibiting a peak around 120° and dropping off asymmetrically on either side of the peak. However, for the 'rejected' fit there is significant discrepancy in the observed anisotropy of P_{T_-} with respect to magnetic orientation. By comparing the anisotropy of the $|T_-\rangle$ probability with the experimental FFT amplitude, we are able to identify an 'optimal' fit from over 50 different possible best fits to the data.

S5 Optimal fit and g-tensor.

Parameter	Optimal Fit	Rejected Fit
t_c	(13.7±0.1)μeV	(14.2±0.1)μeV
$\vec{t}_{so} = (t_x, t_y, t_z)$	(-36.9±2, 107±4, 0 ±10) neV	(-234±5, -295±6, 0±10) neV
$\overleftrightarrow{g}_L$	$\begin{pmatrix} -0.78 & -1.13 & -1.45 \\ -1.13 & 0.85 & -0.27 \\ -1.45 & -0.27 & 1.91 \end{pmatrix}$	$\begin{pmatrix} 0.09 & 0.38 & 0.93 \\ 0.38 & 0.65 & 0.64 \\ 0.93 & 0.64 & -1.56 \end{pmatrix}$
$\overleftrightarrow{g}_R$	$\begin{pmatrix} -0.96 & -0.94 & -1.47 \\ -0.94 & 0.78 & -0.74 \\ -1.47 & -0.74 & 1.82 \end{pmatrix}$	$\begin{pmatrix} 1.26 & -0.42 & 1.22 \\ -0.42 & 0.27 & 1.22 \\ 1.22 & 1.22 & -1.73 \end{pmatrix}$

Table I: Best fit parameters for the Optimal fit and a Rejected fit to the experimentally observed FFT frequencies in Figure 2 of the main text. The best fit procedure allows free fitting to 16 parameters; t_c, t_x, t_y, t_z, 6 parameters for g_L and 6 parameters for g_R. Uncertainty in each of the g-factors was on the order of ± 0.02. As discussed, no unique fit to the level splittings was possible, with more than 50 possible combinations of the free parameters giving good fits. The Optimal fit was determined by additionally considering the $|T_-\rangle$ probability following a 4 ns ramp-in. The optimal fit here is the fit used for the solid lines in Figure 2 of the main text. The rejected fit is one example of a possible fit, which was rejected based on the $|T_-\rangle$ probability analysis.

The parameters for the optimal fit and a rejected fit are presented in Table I.

References

1. Leon C Camenzind, Simon Geyer, Andreas Fuhrer, Richard J Warburton, Dominik M Zumbühl, and Andreas V Kuhlmann. A hole spin qubit in a fin field-effect transistor above 4 kelvin. *Nature Electronics*, 5(3):178–183, 2022.

2. J Robert Johansson, Paul D Nation, and Franco Nori. Qutip: An open-source python framework for the dynamics of open quantum systems. *Computer Physics Communications*, 183(8):1760–1772, 2012.